Automatic detection of calving events from time-lapse imagery at Tunabreen, Svalbard

Dorothée Vallot[1], Sigit Adinugroho[2,3], Robin Strand[3], Penelope How[4], Rickard Pettersson[1], Douglas I. Benn[5], and Nicholas R. J. Hulton[6]

[1]Department of Earth Sciences, Uppsala University, Sweden
[2]Faculty of Computer Science, Brawijaya University, Indonesia
[3]Centre for Image Analysis, Department of Information Technology, Uppsala University, Sweden
[4]Institute of Geography, School of GeoSciences, University of Edinburgh, UK
[5]School of Geography and Geosciences, University St Andrews, Scotland
[6]Department of Arctic Geology, UNIS, The University Center in Svalbard, Norway

Correspondence to: Dorothée Vallot

Abstract.

Calving is an important process in glacier systems terminating in the ocean and more observations are needed to improve our understanding of the undergoing processes and be able to parameterise calving in larger scale models. Time-lapse cameras are good tools for monitoring calving fronts of glaciers and they have been used widely where conditions are favourable.

5 However, automatic image analysis to detect and calculate the size of calving events has not been developed so far. Here, we present a method that fills this gap using image analysis tools. First, the calving front is segmented. Second, changes between two images are detected and a mask is produced to delimit the calving event. Third, we calculate the area given the front and camera positions as well as camera characteristics. To illustrate our method, we analyse two image time series from two cameras placed at different locations in 2014 and 2015 and compare the automatic detection results to a manual detection.

10 We find a good match when the weather is favorable but the method fails with dense fog or high illumination conditions. Furthermore, results show that calving events are more likely to occur (i) close to where subglacial melt water plumes have been observed to rise at the front and (ii) close to one another.

1   Introduction

Tidewater glaciers are one of the main contributors to sea-level rise (Church et al., 2013; Gardner et al., 2013) but the calving

15 process remains difficult to predict and to model. Several studies have focused on finding a calving law (Van der Veen, 2002; Benn et al., 2007; Amundson and Truffer, 2010; Nick et al., 2010; Cook et al., 2012; Krug et al., 2014, 2015) while others are based on improving process-understanding such as melt undercutting (Motyka et al., 2013; Straneo and Heimbach, 2013; Luckman et al., 2015; Rignot et al., 2015; Truffer and Motyka, 2016; Benn et al., 2017; Vallot et al., 2017) and buoyancy-driven calving (Warren et al., 2001; James et al., 2014; Benn et al., 2017). Depending on the external factors or the glacier

20 characteristics, the dominant calving mechanisms can vary. Nonetheless, even though models have become more sophisticated over time, in-situ observations of involved processes at different time scales are essential to calibrate models (Åström et al.,
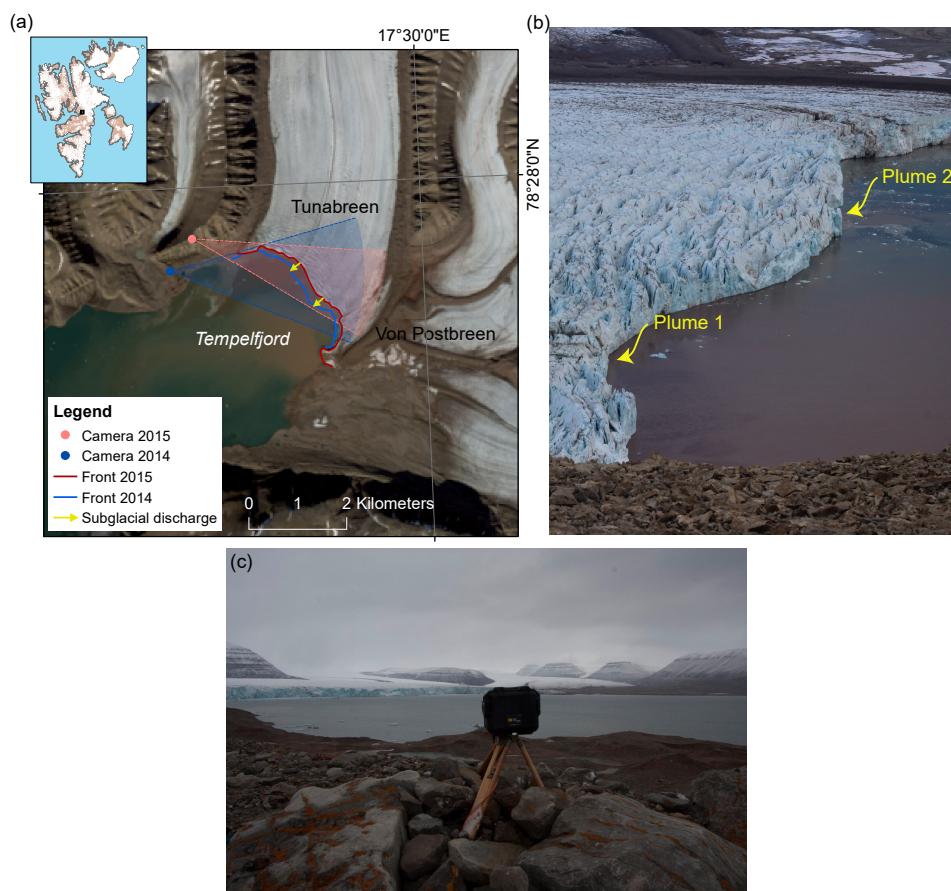
Figure 1. (a) Map of Tunabreen, Svalbard with subglacial discharge positions, time-lapse camera positions and angles of vision. Front position as of September 2014 and August 2015. The satellite image is a Landsat 8 OLI/TIRS C1 Level-1 (14 August 2015). **(b)** Picture taken on August 8, 15:00 showing the two plumes of Tunabreen. **(c)** Time-lapse camera used for 2014 analysis standing in front of Tunabreen.

2013). Chapuis and Tetzlaff (2014) studied the calving events sizes of Kronebreen, Svalbard, and concluded that calving events variability is inherent to calving dynamics even under stable external conditions. Event-size distribution follows a scale-invariant power-law that has been further discussed by Åström et al. (2014), who classify termini of calving glaciers as self-organised critical systems such as earthquakes. They recommended to focus on quantifying the effects of external forcing

5   on the critical state of calving margins, which makes event size and frequency analysis from observation necessary.

     Time-lapse cameras are convenient monitoring tools that have been used for different purposes in glaciology such as daily digital elevation models (James et al., 2014), propagation of flexion zones up-glacier (Murray et al., 2015), glacier velocities (Ahn and Box, 2010; Messerli and Grinsted, 2015; James et al., 2016), monitoring of supraglacial lake levels (Danielson and Sharp, 2013) and meltwater plume surface area (How et al., 2017) or glacier surges (Kristensen and Benn, 2012). Time-lapse

10   imagery has also been used to quantify calving events manually, with different resolution and different scaling methods, for

Columbia glacier, Alaska (Walter et al., 2010), Paierlbreen, Svalbard (Åström et al., 2014), Tunabreen, Svalbard (Åström et al., 2014; Westrin, 2015) and Rink Isbræ, West Greenland (Medrzycka et al., 2016). Alternative approaches have also been used to estimate the size and frequency of calving events at tidewater termini such as direct visual detection (e.g. O'Neel et al., 2007; Bartholomaus et al., 2012; Chapuis and Tetzlaff, 2014), icequake detection (e.g. Bartholomaus et al., 2012; Köhler et al., 2016)

5   or satellite imagery (e.g. Schild and Hamilton, 2013).

To manually detect calving events from time-lapse cameras is a very laborious task that requires days of work and becomes too difficult when the amount of images is too large. For example, if the manual processing of an image takes two minute, the operator would need 17 days (8 hours of work per day) to process a month of images with 10 minutes interval. As a consequence, few studies use the potential of time-lapse cameras and do not analyse more than a few days. Automatic methods

10 have the advantage to enable longer time series but, to date, no satisfying automatic calving detection from time-lapse cameras have been developed.

Here, we utilize a method, first presented by Adinugroho (2015a) and Adinugroho et al. (2015b), to automatically detect calving events from sequential time-lapse imagery. The algorithm follows five main steps in order to achieve this: image registration, segmentation of the calving front, change detection, mask reconstruction and size calculation. The results from this

15 automatic method are compared to a manual detection of calving events to verify and evaluate its accuracy. We use observations from two time-lapse cameras placed at two different locations in front of a tidewater glacier in Svalbard, Tunabreen, during two consecutive summers, 2014 and 2015. The calving event locations at the front are compared to the position of two rising plumes observed at the front and the distribution of event-sizes is compared to a power-law curve.

2   Study area

20 Tunabreen is a 27 km long surging tidewater glacier, draining from the Lomonosovfonna ice cap terminating at the head of Templefjorden in central Svalbard (see Fig. 1). Its drainage area is approximately 174 km^2 (Nuth et al., 2013). This glacier is known to have surged in 1930, 1970 and lately in 2002–2005, experiencing multiple retreats and advances and leaving submarine footprints (Forwick et al., 2010; Flink et al., 2015). It has retreated from its maximum extent, in 2004, until 2016 when it started to surge again. The 3 km wide terminus is roughly 70 m thick and grounded in 40 m deep water (Flink et al.,

25 2015). At the front of Tunabreen, there is one main subglacial drainage portal (see Fig. 1) that can also be seen on the pictures (see Fig. 10 and Fig. 1b). The main subglacial plume, plume 1, is described in detail in Schild et al. (2017). A second subglacial plume, plume 2, less visible, is intermittently present on the pictures (see Fig. 1b). There are also two terrestrial melt-streams, one on each side of the glacier.

3 Methods

3.1 Time-lapse cameras

In 2014, the time-lapse camera was installed in front of Tunabreen calving front, in the moraine field, at the coordinates (N78° 27.084' E17° 16.195' 73 m) as shown in Fig. 1. The camera (Canon EOS 450D) was placed on a tripod in a waterproof
5   plastic box (Pelican Storm IM2075) with a drilled hole in front of the camera (see Fig. 1). The intervalometer is a Digisnap 2700 from Harbortronics with a low temperature modification. The system was powered by a 12 V alkaline battery pack, placed in a plastic box covered by stones. The time interval between pictures was 14 min.

In 2015, an additional time-lapse camera was installed on Ultunafjella, a rock outcrop to the west of the glacier terminus. The camera (Canon EOS 700D) was enclosed in a custom-made peli-case box along with a Harbortronics Digisnap 2700
10   intervalometer. This system was powered by an external 12 V battery and a 10W solar panel. The camera system was installed on a tripod, and the tripod was buried into the ground and anchored by rocks.

Both years, the cameras were set in aperture priority (set aperture value and automatic shutter speed). Camera properties are presented in Table 1.

Table 1. Time-lapse camera properties for 2014 and 2015.

Property	2014	2015
Study time	6 July–6 Sept	19 Aug–7 Sept
Camera	Canon EOS 450D	Canon EOS 700D
Lens	Sigma AF 17–50/2,8	Canon EF 50mm f/1.8 fixed focal length
Filter	UV filter	Polarised filter
Image size	4272×2848 px (12.2 Mpx)	5184×3456 px (18 Mpx)
Sensor size	22.2×14.8 mm	22.3×14.9 mm
Pixel size	5.2 μm	4.3 μm
Aperture	f/2.8	f/16
ISO Speed	ISO-200	ISO-400
Focal length	28 mm	50 mm
Format	.jpg	.jpg
Time interval	14 min	10 min

3.2 Image registration

Detecting changes in a sequence of images requires perfect alignment of the images so that non-moving objects are at the same location for every image in the sequence. However, that condition may not hold in our case. Due to weather conditions, the camera can slightly move and rotate. This may cause false change detection if the images are not geometrically aligned. Thus, image registration is an important step in calving event detection.

Feature-based image registration makes use of shared features on a referenced image and a captured image in order to geometrically align the captured image to the referenced one. Speeded-Up Robust Features (SURF) descriptors (Bay et al., 2008) are extracted from both images. The descriptors from the two images are matched in order to select descriptors existing in both images.

Geometric transformation occurring in two consecutive images can be revealed from a relation between matching descriptors in those images. The M-estimator SAmple Consensus (MSAC) algorithm (Torr and Zisserman, 2000) estimates affine transformation from descriptors, so that the descriptors from the referenced image match most closely with those of the captured image. Based on this transformation model, the captured image can be transformed to geometrically match the reference image.

In Adinugroho et al. (2015b), we registered all images to the first one but this didn't give a good result when the image to register was separated by a long time because the glacier moves and the features in the ocean change. We thus choose to register each image to the previous one. However, when visibility is poor, matching features are scarce and this method does not perform well so we use the registration characteristics of the former image. For the next image, if the visibility is better, we compare with the last good image. We estimate the registration process to perform well above 200 matching features (a normal image counts approximately 2000 features).

3.3 Automatic detection

3.3.1 Segmentation

The first step in automatic detection of calving events is to isolate the calving front from the surroundings to avoid detection of changes at the surface of the glacier or the ocean. First, the image is cropped around the glacier front geometry so that most noise is removed. The cropping region is determined from the first image. Second, we use a region-based active contour method, the Chan-Vese model (Chan and Vese, 2001), to isolate the front and the ocean.

The Chan-Vese model uses a region-based active contour, which works based on region information instead of edge information (boundary detection) as used by an edge-based active contour. We adopt the Chan-Vese model because it does not rely

heavily on edge detection, which is often hard to find between the surface and the front of the glacier. It uses an evolving curve to detect objects in a given image u_0. To do that, the Chan-Vese segmentation minimises an energy function defined as

$$
\begin{aligned}
F(c_1, c_2, C) = {} & \mu \cdot Length(C) + \nu \cdot Area(inside(C)) \\
& + \lambda_1 \int\limits_{inside(C)} |u_0(x,y) - c_1|^2 \, dx \, dy \\
& + \lambda_2 \int\limits_{outside(C)} |u_0(x,y) - c_2|^2 \, dx \, dy,
\end{aligned}
\tag{1}
$$

where μ, ν, λ_1 and λ_2 are non-negative parameters, and C is a curve that separates the image into two regions. c_1 and c_2 denote
5   mean intensity values of the two regions, inside C and outside C, respectively. Eq. 1 reaches its minimum if and only if the curve C lies at the boundary of two homogeneous areas.

At the first iteration, the user is required to delineate two initial masks, around the ocean, M_0^{ocean}, and the front, M_0^{front}, that are iteratively refined using the Chan-Vese model. In order to reduce computation time, the maximum iteration is limited to 50. We want to keep the pixels from the front mask but remove those from the ocean mask. At iteration i, the previous
10   masks, M_{i-1}^{ocean} and M_{i-1}^{front} are used as initial masks of the Chan-Vese model to produce M_i^{front}. Similarly to the registration process, if the visibility is bad we use the mask from the previous iteration.

3.3.2   Change detection

The goal is to detect changes between two grayscale images masked by the intersection of M_{i-1}^{front} and M_i^{front}. Because the luminosity or the weather conditions can have an impact on the change detection, pixel-based change detection methods are not
15   adequate for this study. Instead, a region-based change detection method significantly reduces noise by computing the change of a pixel with respect to its neighbours and thus relying on local structural features (Li and Leung, 2002).

The rotational dependent Local Binary Pattern (LBP) is a simple visual descriptor method to extract the image texture T_i of image i (Ojala et al., 1996, 2002; Pietikäinen et al., 2011). The center pixel, (x_c, y_c), in grayscale value g_c, is compared to its P neighbours values situated at a radius R of coordinates $\{(x_c + R\cos(2\pi p/P), y_c + R\sin(2\pi p/P)), p \in [0, P-1]\}$. The
20   grayscale value, g_p, is linearly interpolated if not falling at the center of a pixel. The texture value of the center pixel (x_c, y_c) is then defined as

$$
T_i(x_c, y_c) = \sum_{p=0}^{P-1} 2^p \delta(g_p - g_c),
\tag{2}
$$

with $\delta(x)$ the Heaviside step function, which gives 0 if $x < 0$ and 1 if $x \geq 0$. Here we use $P = 20$ and $R = 5$ for 2014 and $R = 6$ for 2015. The different values depend on the characteristics of the camera (focal length, distance to the front, resolution,
25   etc.) and the choice is empirical. Parameters P and R have been sampled in $[8, 10, 15, 20, 30, 40]$ and $[5, 10, 15]$ respectively. The quality of the settings has been assessed by comparing errors between the automatic and the manual methods using the

comparison metric presented in subsection 3.5. For both year, best results were achieved with $P = 20$ disregarding the value of R. The value of the radius R is sensitive to the size of the image pixel.

To determine the amount of change in the texture of two consecutive images, we use the Combined Difference Image and K-means clustering (CDI-K) as proposed by Zheng et al. (2014). Two operators, the absolute difference and the logarithmic

5 difference, are applied to the texture images T_{i-1} and T_i, and produce two change-images, D_s and D_t respectively

$$D_s = |T_{i-1} - T_i|, \tag{3}$$
$$D_t = |\log(T_{i-1}) - \log(T_i)|. \tag{4}$$

The change-images are normalised to the range $[0, 255]$. We then apply a mean filter (11×11) to D_s in order to remove isolated pixels and a median filter (3×3) to D_t in order to remove isolated pixels but preserve edges. The resulting images, D'_s and D'_t

10 are combined, the former achieving sleekness and the latter maintaining edge information, using a weight parameter $w > 0$

$$D = wD'_s + (1 - w)D'_t. \tag{5}$$

We set the weight parameter $w = 0.1$ as suggested by Zheng et al. (2014).

To decide if there is change or no-change, we choose to use a local neighbour threshold because of its deterministic nature in contrast with the randomness of K-means. A median function is applied to D on a 25×25 pixel window.

15 When the weather is too foggy in one image, the whole calving front is detected as calved and it takes a long time for the algorithm to perform. We therefore remove images that are falling in this category by calculating the coefficient of variation (CV) of the calving front, which gives an idea of the intensity distribution of the image. If the CV is above or below a certain threshold, determined beforehand from a set of images, the image is removed. The threshold has been determined by comparing errors between manual and automatic methods using the comparison metric presented in subsection 3.5. Above the threshold,

20 the image is highly illuminated and below the threshold, the image is covered by dense fog. The front is almost not recognisable so calculation is impossible and errors are systematically very large and the size of the automatically detected calving events is close to the size of the front.

3.3.3 Change mask reconstruction

The end product of the change detection method detailed above is generally a set of clustered points of change (see Fig. 2a)

25 and we use a mask reconstruction method, called the α-shape method (Edelsbrunner et al., 1983), to transform the result into polygons (see Fig. 2b). We can determine the set of points situated on the boundary of any empty open disk of radius α (the points situated on the blue curve in Fig. 3). The polygon is then constructed from these points (in red in Fig. 3). α is a very sensitive parameter and has to be chosen with care. If α tends towards zero, only the points themselves are kept. The smaller is α, the smaller are the empty open disks around the points and the smaller is the α-shape (the reconstructed area). If α

30 tends towards infinity, the α-shape is the convex-hull of the points. We further test the sensitivity of the mask reconstruction parameter α.
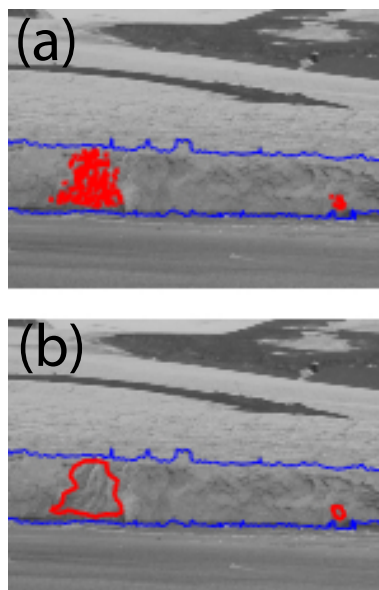
Figure 2. **(a)** Clustered points where change has been detected using the method described in section 3.3.2. **(b)** Mask reconstruction using the method described in section 3.3.3, which transforms the clustered points into polygons.
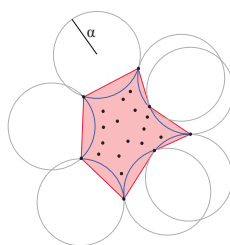
Figure 3. Schematic of the mask reconstruction using the $alpha$-shape method.

A polygon is kept if the number of pixels it contains is higher than a threshold otherwise it is considered as noise. The size threshold depends on the real size of the pixels (described in the next section). To simplify, we use the real size of a pixel averaged over the whole front and a threshold of $50\,\mathrm{m}^2$.

3.4 Size calculation

5 To estimate the pixel size we use the photogrammetric concept that the real pixel size is dependent on the focal length of the camera, the distance from camera to the front and the physical size of the pixel at the sensor. The distance to the front is calculated from georeferenced satellite images Landsat 8 OLI/TIRS C1 Level-1 downloaded from USGS EROS (ten images from July–September 2014 and one image from August 2015).The real pixel area of the image pixel (x_i, y_i) is $A_i = d_X^i \times d_Z^i$ where d_X^i and d_Z^i are the real lengths of the pixel in the horizontal and vertical directions of the image, respectively (see Fig. 4).
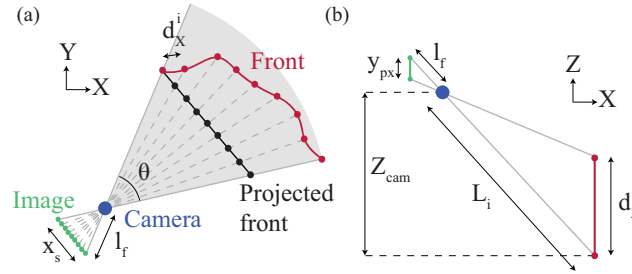
Figure 4. Schematic of the size calculation **(a)** in the horizontal direction and **(b)** in the vertical direction.

The front is outlined with a user control tool in the image so we can determine the distance of the front in pixels, d. We outline the front on the satellite image and project it into the camera horizontal direction (black line in Fig. 4a) to get a number of d evenly distributed points. When projected back to the front (red line in Fig. 4a), the distance between each point (X_i, Y_i) is the real pixel size in the horizontal direction. To perform the projection we use reference points on the front, camera position

5   (X_{cam}, Y_{cam}) and the focal angle $\theta = 2\arctan(x_s/(2l_f))$ where x_s is the sensor size in the horizontal direction and l_f is the focal length (see Table 1). In the vertical direction, we assume a vertical front and calculate the distance, L_i, from the camera to the front. We assume no distortion of the projected pixels in the vertical direction so that each pixel on a vertical column has the same size (same distance from the camera) and we correct for the elevation, Z_{cam}, of the camera location. The real size of the pixel in the vertical direction, d_Z^i, is then

10   $$d_Z^i = \frac{L_i}{l_f} y_{px},$$ (6)

where $L_i = ((X_{cam} - X_i)^2 + (Y_{cam} - Y_i)^2 + Z_{cam}^2)^{1/2}$ is the distance from the camera to the front at the sea-level and y_px is the real size of a pixel in the y-direction. Lens distortions are neglected here. Given the radial distortion coefficients of the lens, the focal length and the pixel size, the distortion error for the front pixel situated the farthest from the camera was smaller than 0.2 % for both lenses.

15   **3.5   Comparison with manual method**

In order to assess the performance of the automatic detection method, we compare the results to a manual method on the same set of images using human visual detection. This does not give the absolute accuracy of the method in relation to true calving since this would require an independent dataset. In 2014, 1100 images were used for comparison of the automatic detection for the period 26 August to 6 September. In 2015, 469 images were used for the period 1 September to 4 September.

20   **3.5.1   Visual detection**

Visual detection of calving events is performed by comparing two consecutive images. It is possible to zoom to a certain section of the glacier and switch from one picture to another to visually detect a change in the glacier front texture. A detected change,

which represents a calving event, is outlined manually and the coordinates are saved. The manual detection for 2014 has been performed by Westrin (2015).

3.5.2 Comparison metrics

The location and size of each calving event are the main results we want to retrieve. For the location, we construct a confusion matrix, which gives the agreements and disagreements between the automatic and the visual detection for each pair of masked images (e.g. Stehman, 1997) and which contains:

- True positives (TP) is the number of pixels labeled as calved in both detections,

- False positives (FP) is the number of pixels labeled as calved in the automatic detection but not in the visual detection,

- True negatives (TN) is the number of pixels labeled as non-calved in both detections,

- False negatives (FN) is the number of pixels labeled as calved in the visual detection but not in the automatic detection.

The number of pixels automatically detected as calved and non-calved are $P_{auto} = TP + FP$ and $N_{auto} = TN + FN$ respectively. The number of pixels visually detected as calved and non-calved are $P_{visual} = TP + FN$ and $N_{visual} = TN + FP$. The total number of pixels is $m = TP + FP + TN + FN$. It is important to note that, for the case of glacier such as Tunabreen with limited calving event size, the number of pixels labeled as calved is generally small compared to non-calved pixels. In this sense, the accuracy measure $Acc = (TP + TN)/m$ is not appropriate since $TP << TN$ as stated by Kubat et al. (1998) for imbalance classes. Here we need a method to detect changed regions, instead of unchanged ones. They recommend the use of F-measure to measure a classification problem with imbalanced classes. However, F-measure has a property that is invariant under the change of TN (Kubat et al., 1998), thus it is less sensitive to changes in unchanged pixels. Alternatively, the Matthews correlation coefficient (Matthews, 1975),

$$Mcc = \frac{TP \times TN - FP \times FN}{\sqrt{P_{auto} \times P_{visual} \times N_{visual} \times N_{auto}}}, \tag{7}$$

is a better measure for imbalanced classes and it takes into account both true and false positive. Its interpretation is similar to the Pearson correlation coefficient between the observed and predicted binary classifications. A value of +1 represents perfect match while -1 total disagreement. Perfect match is only happening when no change is detected by both methods. When there is no overlapping or a calving event is only detected by one of the methods, the Mcc will give a low value by definition whatever the size of the detected event. To be able to compare the magnitude of the error, we can look at the positive difference as the difference between detected calved zones from both methods divided by the total number of pixels,

$$P_{diff} = \frac{P_{auto} - P_{visual}}{m}, \tag{8}$$

to assess the importance of the mismatch.

The weather conditions and illumination change the pixel intensities and can inhibit detection in some cases. We determined five categories: Normal conditions (N), light fog (LF), dense fog (DF), high illumination (HI) and low illumination (LI).
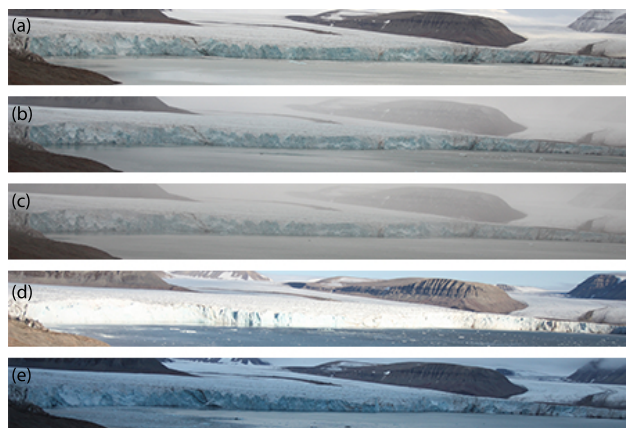
Figure 5. Weather conditions and illumination categories: **(a)** normal (N), **(b)** light fog (LF), **(c)** dense fog, **(d)** high illumination, and **(e)** low illumination.
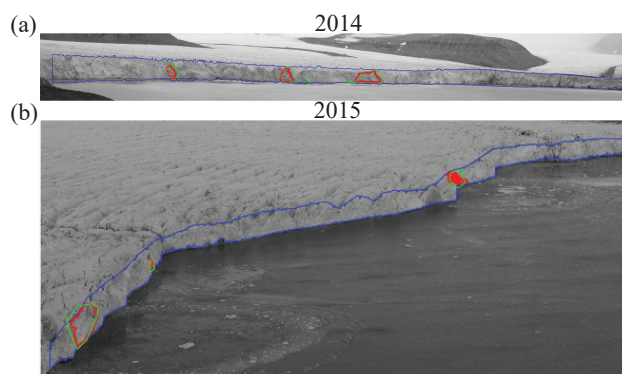
Figure 6. Example of mask delineation (blue), automatic calving detection (red) and manual calving detection (green) for **(a)** 2014 (September 2, 11:45), and **(b)** 2015 (September 1, 19:21).

Some examples are shown in Fig. 5. When comparing manual and automatic detection, we visually determine the categories qualitatively. Each image has also been cut in six different sections placed in a weather condition category.

4   Results

4.1   Comparison assessment

5   An example of calving detection from the automatic and manual methods is shown in Fig. 6.

Different weather conditions have been studied at six different sections of the glacier (see Fig. 10) and the Mcc and P_{diff} is shown in Fig. 7 for 2014 (a) and 2015 (b). We chose not to show the perfect match $Mcc = 1$, corresponding to no detection of calving for both methods on the figure because a fairly large number of images do not have calving and it skews the results
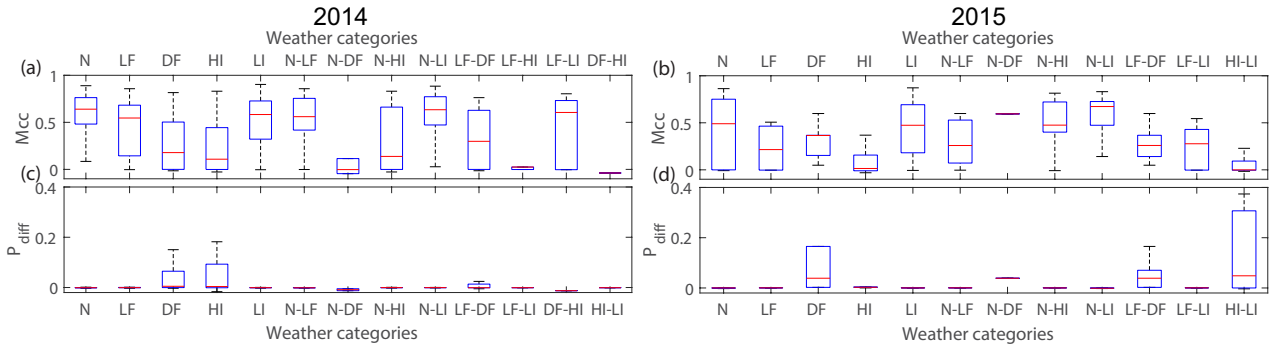
Figure 7. Box plot of Matthews correlation coefficient, Mcc, when $Mcc \neq 0$ and $Mcc \neq 1$ for **(a)** 2014 and, **(b)** 2015. Positive difference percentage, P_{diff}, when $Mcc = 0$ (no matched pixel) for normal condition (N), light fog (LF), dense fog (DF), high illumination (HI) and low illumination (LI) and a combination of each for **(c)** 2014, and **(d)** 2015.
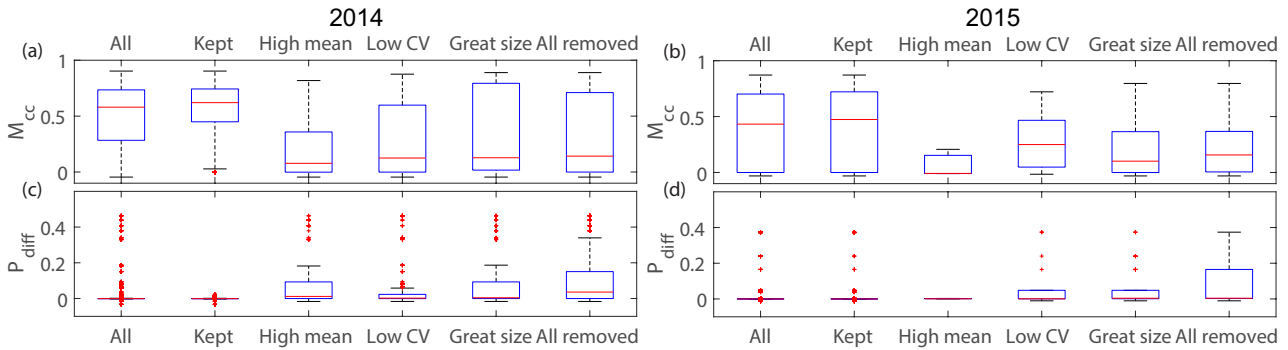
Figure 8. (a) Box plot of Matthews correlation coefficient, Mcc, when $Mcc \neq 0$ and $Mcc \neq 1$ and **(b)** positive difference percentage, P_{diff}, when $Mcc = 0$ (no matched pixel) for all images, for the images kept and for the images removed from high intensity mean, low intensity coefficient of variation (CV) or size thresholds.

towards 1. Instead, we chose to show the percentage of occurrences where $Mcc = 1$ in Table 2. To assess the errors, we use the Mcc when there are matching pixels between both detection ($Mcc \neq 0$) and P_{diff} otherwise ($Mcc = 0$). In general, normal conditions (N), light fog (LF) and low illumination (LI) or a combination of these conditions have a high Mcc with a mean close to 0.7 (2014) or 0.5 (2015) and can be considered as good matches. When $Mcc = 0$, the difference between pixels, P_{diff}
5 is close to zero. On the contrary, dense fog (DF), high illumination (HI) conditions and any combination with one or the other show a relatively low Mcc and high P_{diff} particularly. If such a configuration is combined with any of the others, the result is also poor.

We decided to remove all pictures with high illumination and dense fog from the analysis. To determine whether a picture is falling in this category, we look at the standard deviation and mean of pixel intensity for each section of the image after
10 calibrating these values for normal conditions on a set of images. Pictures with high mean intensity compared to normal

Table 2. Percentage of $Mcc = 1$ for each weather category.

Category	N	LF	DF	HI	LI	N–LF	N–DF	N–HI	N–LI	LF–DF	LF–HI	LF–LI	DF–HI	HI–LI
2014	9.81%	0.67%	0.42%	0.74%	4.23%	1.14%	0.03%	0.31%	1.11%	0.33%	0.06%	0.09%	0%	0.02%
2015	21.60%	0.11%	0.28%	0.46%	10.71%	0.04%	0.14%	0.43%	3.23%	0.25%	0%	0%	0%	0.18%

range for each section fall into high illumination category. Pictures with low CV (ratio between standard deviation and mean intensity) fall into dense fog category. Moreover, given the calving characteristics of Tunabreen (generally no glacier-wide calving events), we assume that if the detected calving size is greater than a certain value depending on the front size, the detection is not satisfactory and we thus remove it from the results. Fig. 8 shows the results for 2014 and 2015. This method

5 has limitations since even if it performs well at removing bad detection, it also removes good ones.

To test the sensitivity of the mask reconstruction parameter α, we look at five different values and compare the results after removing unfavorable weather. This is shown in Fig. 9. If α is too small, the event sizes from the automatic detection tend to be smaller than from the manual detection and vice-versa for too big α. In Fig. 9, the best fit between manual and automatic detected calving events is when $\alpha = 10$ given the Mcc and P_{diff} results.
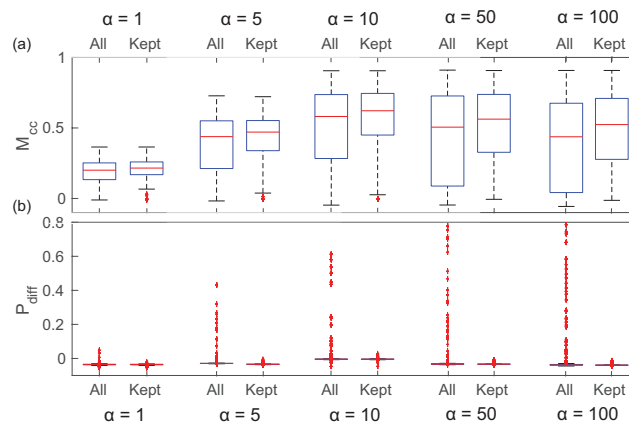
Figure 9. **(a)** Box plot of Matthews correlation coefficient, Mcc, when $Mcc \neq 0$ and $Mcc \neq 1$ and **(b)** positive difference percentage, P_{diff}, when $Mcc = 0$ (no matched pixel) for all images and for the images kept given different values of the mask reconstruction parameter α.

10 ## 4.2 Calving detection

The initial number of pictures to be analysed in 2014 was 6292 but because of weather conditions and camera settings, only 3497 usable images remain, of which 2084 showed no calving. In total, 2575 calving events have been detected ranging from 20 to 3500 m^2. An example of mask delineation and calving detection is given in Fig. 10a. To facilitate the analysis, the front is divided in six sections as shown in Fig. 10a. The number of calving events detected in each section is 524 in section 1, 681

15 in section 2, 455 in section 3, 341 in section 4, 344 in section 5 and 230 in section 6.
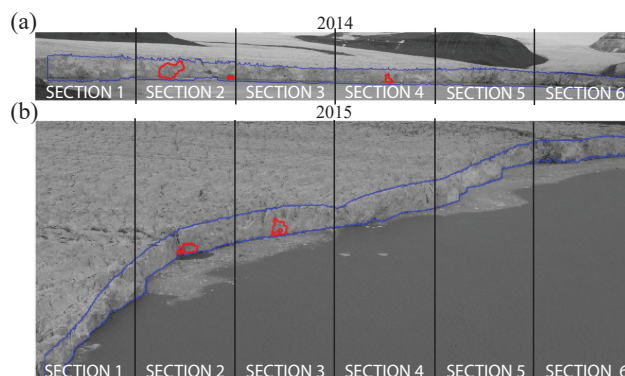
Figure 10. Example of mask delineation (blue) and calving detection (red) for **(a)** 2014 (September 4, 16:01) and **(b)** 2015 (August 19, 19:10). The front is divided into six sections shown on the figures.

In 2015 3242 images were analysed, but 571 of these were removed as the glacier terminus was obscured by water droplets on the porthole cover of the time-lapse enclosure. Because of this, there is no coverage between 23–27 August. After weather filtering, 1495 images are left including 898 with no calving detection. In total, 1647 events were detected (222 in section 1, 327 in section 2, 228 in section 3, 234 in section 4, 398 in section 5 and 238 in section 6). An example of mask delineation and calving detection is given in Fig. 10b.

4.3 Spatio-temporal size distribution

In Fig. 11, we present the total area detected per image (in blue) and the daily moving average (in red). It is difficult to establish seasonal pattern because of the data gaps during unfavorable weather conditions.
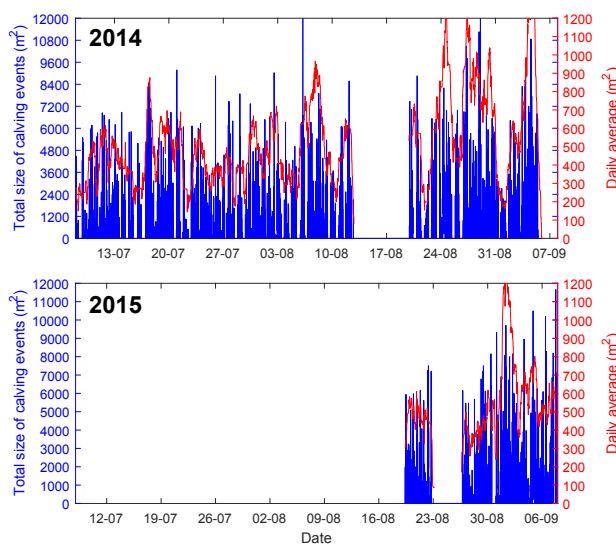
Figure 11. Total size detected per image (in m^2) in blue and moving average on a daily basis (in m^2) in red for **(a)** 2014, and **(b)** 2015.

Instead, we explore the relative size distribution for the different sections to estimate which section undergoes the largest calving events per image (see Fig. 12a–c). When calving events are detected on an image, we look at the size proportion of each section. If, for a pair of images, calving is detected in only one section, this section gets 100% of the total. If other events occur within the same time frame in other sections, these sections get a proportional fraction corresponding to their size compared with the total calved size of the whole calving front. The primary event section receives the largest share. In Fig. 12b–d, for each primary event section, we show the share of the secondary event.

If a section gets 100% of the total size during a time frame, it is more often section 2, followed by section 5, in 2014, whereas, in 2015, it is more often section 5 followed by section 2. In general, section 2 for 2014 and section 5 for 2015 have the most occurrences of primary calving event size. Also, when primary calving event size occurs in section 5, secondary calving occurs particularly in section 2. For 2015, section 5 is also secondary when section 2 is primary. It is also where the most margin retreat occurs in the season. Furthermore, there seems to be a link between sections. When a primary calving event occurs in a section, secondary calving event sizes are usually found in adjacent sections.

4.4 Event-size distribution

Fig. 13 shows the event-size relative abundance distributions for both years. The relative abundance $n(A)$ is the ratio between the frequency and the sample size of calving areas A. The black curve is a power-law estimate of exponent -1.2 for 2014 with smaller sizes have been removed from the distribution. There is a cut-off for large sizes around 5×10^3 m^2.
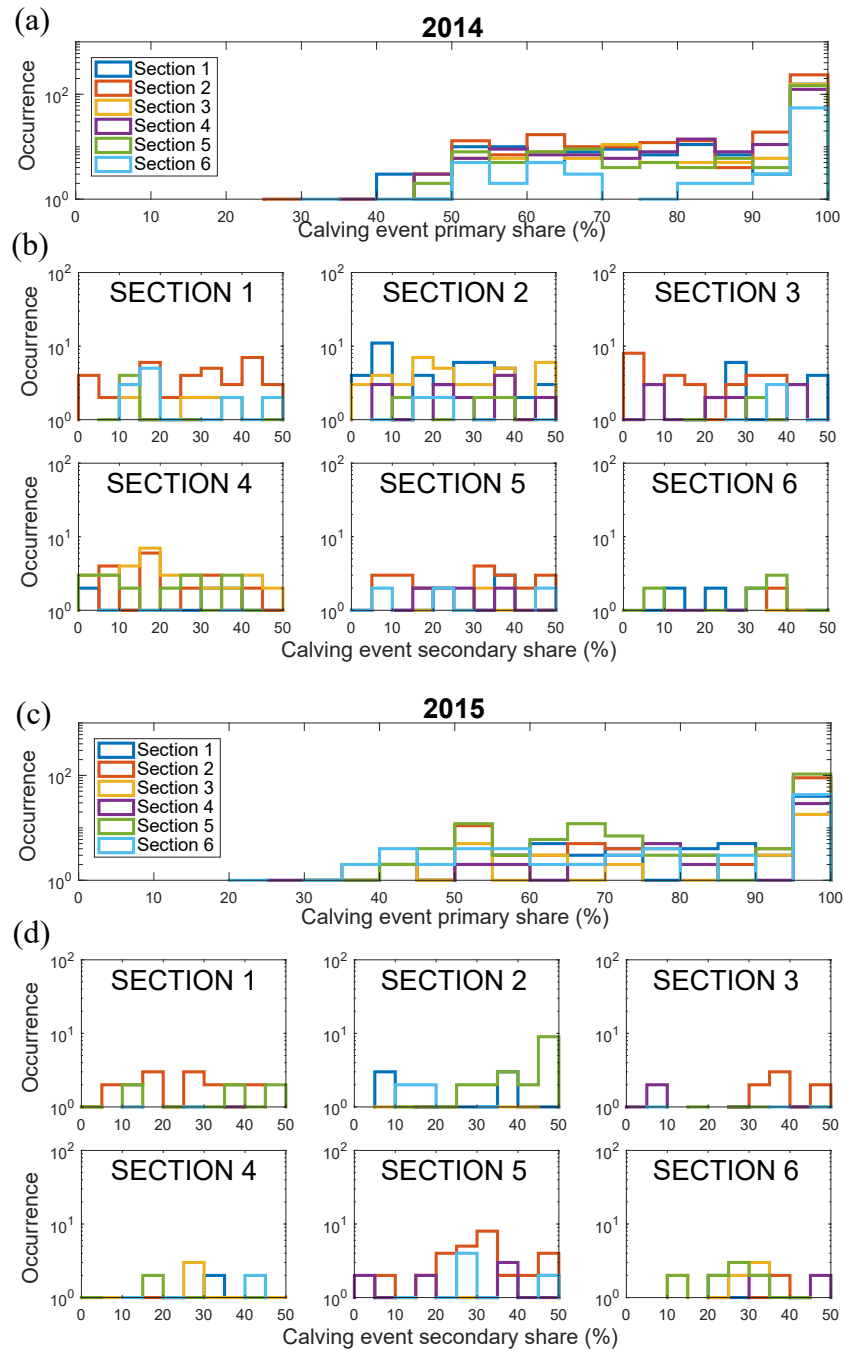
Figure 12. Size proportion histogram of the major calving event size per image for **(a)** 2014, and **(c)** 2015. Size proportion histogram of the secondary calving event size per image and per section for **(b)** 2014, and **(d)** 2015.
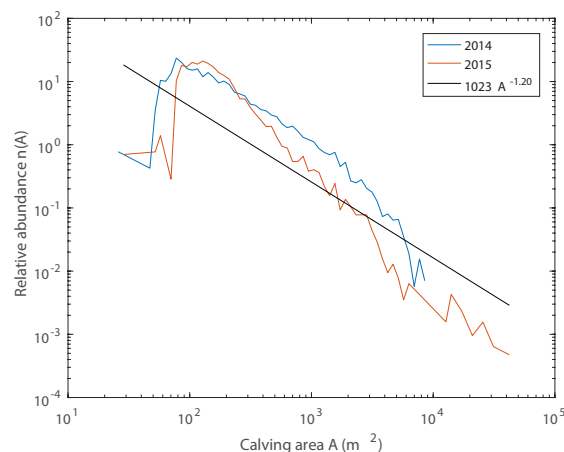
Figure 13. Relative abundance distribution $n(A)$ of calving areas A for 2014 and 2015. The black curve is a power-law estimate of exponent -1.2.

5 Discussion and conclusion

5.1 Calving, plumes and self-organised criticality

The spatio-temporal information such a method provides has the potential to enhance understanding of certain processes or validate calving theories. Here we used two time series of two different years from two different locations and camera settings. Some problems still need to be addressed and are discussed in the following section. The long time-lapse and the weather-related issues do not allow direct conclusion on the spatio-temporal calving behaviour of Tunabreen. Still, it appears that most of the large calving events happened near plume locations (sections 2 and 5) with larger events at the most active plume location, plume 1 (section 2). The plume in section 5 has not been detected elsewhere in the literature so this conclusion has to be taken with care and this should be investigated further. It also appears that when a large event is triggered at the less active plume location, plume 2 (section 5), a smaller one is simultaneously triggered at of plume 1. Moreover, events in one section seem to trigger smaller events in adjacent sections, which confirms the destabilisation of the local neighborhood of the calving region observed by Chapuis and Tetzlaff (2014).

A self-organised critical (SOC) system in nature, is a system that exhibits a slow and steady accumulation of an instability followed by a rapid relaxation triggered from a single point and, independently to external conditions, leading to the collapse of any possible size (Jensen, 1998). Åström et al. (2014) showed that the calving front behaviour of tidewater glaciers had the characteristics of an Abelian sandpile model, a simple SOC system (Dhar, 1999). The probability distribution at the critical point approaches a power-law with an exponent close to -1.2, which is also the case for the results showed in Fig. 13. Cut-offs for large sizes have also been reported in Åström et al. (2014) for smaller glaciers and they are due to the glacier front size. For smaller sizes, the relative abundance is below the power-law estimate. This is due either to the long time-lapse between images

that does not allow small events to be detected, or to the spatial resolution of the camera. The system always tends towards criticality without regard to external factors. However, external conditions have the potential to change the system from sub- to supercritical. Investigation of relationship between calving events and environmental controls will be the subject of a separate paper.

5.2 Errors and limitations

The main limitation is clearly the poor performances due to the weather: in presence of fog or when the calving terminus is strongly illuminated by the sun. The illumination problem is worst during daytime when the sun is reflected on the ice. At those times, mostly in the middle of the day, the temperature is high leading to surface melt, subglacial discharge and active plume. The marine melt feedback is therefore difficult to analyse with this method if the weather condition problem is not solved. Nevertheless, in normal conditions or low illumination, the method performs well compared with the manual method and is a good tool to assess the location of the calving events. Errors in detection, however, may arise because of different factors. First, the method requires different parameters at each step and most of them are defined empirically (trial and error), particularly the change detection and mask recognition parameters but also the threshold for unfavorable weather condition and minimum/maximum calving size. Second, the method detects frontal changes and is not able to recognise external objects coming into view of the camera, such as birds or icebergs, nor make the difference between frontal ice changing position, because of gravity for example, and actual calving. Third, while the glacier front calves, it also advances due to ice flow and both processes have an effect on the front position. Because of that, the front outline needs to be manually refined periodically, depending on the flow speed of the glacier and the camera view angle. For Tunabreen, refinement was needed every 1000 pictures or every 8–10 days. Fourth, no subaqueous calving can be detected with this method although, for certain glaciers, this could account for a large proportion of the frontal mass loss. Finally, the manual detection is subject to error because of a failure to correctly identify or digitise events.

5.3 Recommendations and future improvements

Despite inherent limitations, the method can still be improved. First, the camera settings and camera installation have an impact on the result and can be optimised. For the setup in 2014, the large aperture setting (f/2.8) and the lack of polarised filter rendered more pictures compared to 2015 to fall into the HI category. It is important to consider all situations the automatic settings of the camera will have to handle. Also, instead of fixing the aperture width, one could fix the aperture speed to let the lens adapt to the amount of light available or adapt the ISO, as in Kwasnitschka et al. (2016).The position of the camera also influences the results and our two different camera locations show both benefits and drawbacks. A camera positioned at low elevation and in front of the glacier (2014) is favourable for the segmentation (refinement has to be done less often) whereas a camera situated more to the side and at higher elevation (2015) is favourable to recognise larger events but parts of the front may be occluded. In some images, calving events are recorded at different locations and having a shorter time-lapse interval (to be set according to the characteristics of the glacier) could help to distinguish single events. Storing the images in lossy file format (like .jpg) also certainly degrades the quality and the ability to record events. Depending on how often the memory card

can be changed or if there is a service of automatic downloading of images, it would help to store the pictures in raw format so that more postprocessing is available.

Second, the method can be improved in detecting or enhancing images with unfavorable weather. Fog detection is implemented for different applications (e.g. automatic car navigation) and could be useful (e.g. Hautière et al., 2014). If weather observations are available, it can also be good to combine these data to detect total whiteout of an area for example (Jiskoot et al., 2015).

Third, the size calculation only gives the 2-dimensional area of the calving event and a third dimension could be calibrated from observation (Chapuis and Tetzlaff, 2014) or from other cameras placed at different locations. Moreover, the distance between the camera and the front is estimated from satellite data with rather low spatio-temporal resolution and data with higher resolution could improve the size calculation (e.g. satellite, other time-lapse cameras or unmanned aerial vehicle photogrammetry).

This automatic method has been developed for a particular glacier, Tunabreen, but can be calibrated for other glaciers, even if the spatio-temporal scale is different. For instance, glaciers in Greenland, where calved icebergs are larger and detached more often, are a good candidate. Time-lapse cameras are easy to place in front of a glacier to monitor the calving state of it and this method can help to automatise an otherwise difficult task.

Author contributions. DV and RP have designed and constructed the time-lapse cameras for 2014. PH and NH have designed the time-lapse camera for 2015. DV, RP, NH, DB and PH have co-ordinated the camera deployment and collected the memory cards. SA, RS and DV have developed the automatic detection and DV the manual detection. DV manually detected calving events from the 2015 record. DV has written the main section of the article and all authors have contributed.

Acknowledgements. Landsat data available from the U.S. Geological Survey are used in this study. The 2015 time-lapse camera was constructed by Alex Hart and the GeoSciences workshop at the University of Edinburgh. We thank Heidi Sevestre, Chris Bortstad, Sergey Marchenko, Elena Marchenko, Anne Flink, Pontus Westrin and Silje Smith-Johnsen for their help to place the cameras. We thank Ymer-80, the Swedish Society for Anthropology and Geography (SSAG) and the Wallenberg foundation for their economical support for the camera deployment in 2014. The time-lapse camera deployment in 2015 was funded by the Conoco Phillips-Lundin Northern Area Program through the CRIOS project (Calving Rates and Impact On Sea level, RiS-ID 6155).

References

Adinugroho, S.: Calving Events Detection and Quantification from Time-lapse Images : A Case Study of Tunabreen Glacier, Svalbard, Master's thesis, Uppsala University, Department of Information Technology, 2015a.

Adinugroho, S., Vallot, D., Westrin, P., and Strand, R.: Calving Events Detection and Quantification from Time-lapse Images in Tunabreen Glacier, in: 2015 International Conference on information & Communication technology and systems (ICTS), IEEE, Surabaya, September 16th, doi:10.1109/ICTS.2015.7379872, 2015b.

Ahn, Y. and Box, J. E.: Glacier velocities from time-lapse photos: technique development and first results from the Extreme Ice Survey (EIS) in Greenland, Journal of Glaciology, 56, 723–734, doi:10.3189/002214310793146313, 2010.

Amundson, J. M. and Truffer, M.: A unifying framework for iceberg-calving models, Journal of Glaciology, 56, 822–830, doi:10.3189/002214310794457173, 2010.

Åström, J. A., Riikilä, T. I., Tallinen, T., Zwinger, T., Benn, D., Moore, J. C., and Timonen, J.: A particle based simulation model for glacier dynamics, Cryosphere, 7, 1591–1602, doi:10.5194/tc-7-1591-2013, 2013.

Åström, J. A., Vallot, D., Schäfer, M., Welty, E. Z., O'Neel, S., Bartholomaus, T., Liu, Y., Riikilä, T., Zwinger, T., Timonen, J., et al.: Termini of calving glaciers as self-organized critical systems, Nature Geoscience, 7, 874–878, doi:10.1038/NGEO2290, 2014.

Bartholomaus, T. C., Larsen, C. F., O'Neel, S., and West, M. E.: Calving seismicity from iceberg-sea surface interactions, Journal of Geophysical Research: Earth Surface, 117, doi:10.1029/2012JF002513, 2012.

Bay, H., Ess, A., Tuytelaars, T., and Gool, L. V.: Speeded-Up Robust Features (SURF), Computer Vision and Image Understanding, 110, 346–359, doi:10.1016/j.cviu.2007.09.014, similarity Matching in Computer Vision and Multimedia, 2008.

Benn, D. I., Warren, C. R., and Mottram, R. H.: Calving processes and the dynamics of calving glaciers, Earth-Science Reviews, 82, 143–179, doi:10.1016/j.earscirev.2007.02.002, 2007.

Benn, D. I., Åström, J., Zwinger, T., Todd, J., Nick, F. M., Cook, S., Hulton, N. R., and Luckman, A.: Melt-under-cutting and buoyancy-driven calving from tidewater glaciers: new insights from discrete element and continuum model simulations, Journal of Glaciology, pp. 1–12, doi:10.1017/jog.2017.41, 2017.

Chan, T. F. and Vese, L. A.: Active contours without edges, IEEE Transactions on image processing, 10, 266–277, doi:10.1109/83.902291, 2001.

Chapuis, A. and Tetzlaff, T.: The variability of tidewater-glacier calving: origin of event-size and interval distributions, Journal of glaciology, 60, 622–634, doi:10.3189/2014JoG13J215, 2014.

Church, J., Clark, P., Cazenave, A., Gregory, J., Jevrejeva, S., Levermann, A., Merrifield, M., Milne, G., Nerem, R., Nunn, P., Payne, A., Pfeffer, W., Stammer, D., and Unnikrishnan, A.: Sea Level Change, book section 13, pp. 1137–1216, Cambridge University Press, Cambridge, United Kingdom and New York, NY, USA, doi:10.1017/CBO9781107415324.026, 2013.

Cook, S., Zwinger, T., Rutt, I., O'Neel, S., and Murray, T.: Testing the effect of water in crevasses on a physically based calving model, Annals of Glaciology, 53, 90–96, doi:10.3189/2012AoG60A107, 2012.

Danielson, B. and Sharp, M.: Development and application of a time-lapse photograph analysis method to investigate the link between tidewater glacier flow variations and supraglacial lake drainage events, Journal of Glaciology, 59, 287–302, doi:10.3189/2013JoG12J108, 2013.

Dhar, D.: The Abelian Sandpile and Related Models, Physica A Statistical Mechanics and its Applications, 263, 4–25, doi:10.1016/S0378-4371(98)00493-2, 1999.

Edelsbrunner, H., Kirkpatrick, D., and Seidel, R.: On the shape of a set of points in the plane, IEEE Transactions on information theory, 29, 551–559, doi:10.1109/TIT.1983.1056714, 1983.

Flink, A. E., Noormets, R., Kirchner, N., Benn, D. I., Luckman, A., and Lovell, H.: The evolution of a submarine land-form record following recent and multiple surges of Tunabreen glacier, Svalbard, Quaternary Science Reviews, 108, 37 – 50,
5   doi:10.1016/j.quascirev.2014.11.006, 2015.

Forwick, M., Vorren, T. O., Hald, M., Korsun, S., Roh, Y., Vogt, C., and Yoo, K.-C.: Spatial and temporal influence of glaciers and rivers on the sedimentary environment in Sassenfjorden and Tempelfjorden, Spitsbergen, Geological Society, London, Special Publications, 344, 163–193, doi:10.1144/SP344.13, 2010.

Gardner, A. S., Moholdt, G., Cogley, J. G., Wouters, B., Arendt, A. A., Wahr, J., Berthier, E., Hock, R., Pfeffer, W. T., Kaser, G., et al.: A
10   reconciled estimate of glacier contributions to sea level rise: 2003 to 2009, science, 340, 852–857, doi:10.1126/science.1234532, 2013.

Hautière, N., Tarel, J., and Halmaoui, H.: Enhanced fog detection and free-space segmentation for car navigation, Machine Vision and Applications, doi:10.1007/s00138-011-0383-3, 2014.

How, P., Benn, D. I., Hulton, N. R. J., Hubbard, B., Luckman, A., Sevestre, H., Van Pelt, W. J. J., Lïndback, K., Kohler, J., and Boot, W.: Rapidly changing subglacial hydrological pathways at a tidewater glacier revealed through simultaneous observations of water pressure,
15   supraglacial lakes, meltwater plumes and surface velocities, The Cryosphere, 11, 2691–2710, doi:10.5194/tc-11-2691-2017, 2017.

James, M. R., How, P., and Wynn, P. M.: Pointcatcher software: analysis of glacial time-lapse photography and integration with multitemporal digital elevation models, Journal of Glaciology, 62, 159–169, doi:10.1017/jog.2016.27, 2016.

James, T. D., Murray, T., Selmes, N., Scharrer, K., and O'Leary, M.: Buoyant flexure and basal crevassing in dynamic mass loss at Helheim Glacier, Nature Geoscience, 7, 593, doi:10.1038/ngeo2204, 2014.

20 Jensen, H. J.: Self-organized criticality: Emergent complex behavior in physical and biological systems, vol. 10, Cambridge university press, 1998.

Jiskoot, H., Harvey, T., and Gilson, G.: Arctic Coastal Fog over Greenland Glaciers using an Improved MODIS Fog Detection Method and Ground Observations, 2015.

Köhler, A., Nuth, C., Kohler, J., Berthier, E., Weidle, C., and Schweitzer, J.: A 15 year record of frontal glacier ablation rates estimated from
25   seismic data, Geophysical Research Letters, 43, 12,155–12,164, doi:10.1002/2016GL070589, 2016.

Kristensen, L. and Benn, D.: A surge of the glaciers Skobreen–Paulabreen, Svalbard, observed by time-lapse photographs and remote sensing data, Polar Research, 31, 11 106, doi:10.3402/polar.v31i0.11106, 2012.

Krug, J., Weiss, J., Gagliardini, O., and Durand, G.: Combining damage and fracture mechanics to model calving, The Cryosphere, 8, 2101–2117, doi:10.5194/tcd-8-1631-2014, 2014.

30 Krug, J., Durand, G., Gagliardini, O., and Weiss, J.: Modelling the impact of submarine frontal melting and ice mélange on glacier dynamics, The Cryosphere, 9, 989–1003, doi:10.5194/tc-9-989-2015, 2015.

Kubat, M., Holte, R. C., and Matwin, S.: Machine Learning for the Detection of Oil Spills in Satellite Radar Images, Machine Learning, 30, 195–215, doi:10.1023/A:1007452223027, 1998.

Kwasnitschka, T., Köser, K., Sticklus, J., Rothenbeck, M., Weiß, T., Wenzlaff, E., Schoening, T., Triebe, L., Steinführer, A., Devey, C. W.,
35   and Greinert, J.: DeepSurveyCam - A Deep Ocean Optical Mapping System, Sensors, 16 2, 164, 2016.

Li, L. and Leung, M. K.: Integrating intensity and texture differences for robust change detection, IEEE Transactions on image processing, 11, 105–112, doi:10.1109/83.982818, 2002.

Luckman, A., Benn, D. I., Cottier, F., Bevan, S., Nilsen, F., and Inall, M.: Calving rates at tidewater glaciers vary strongly with ocean temperature, Nature communications, 6, doi:10.1038/ncomms9566, 2015.

Matthews, B.: Comparison of the predicted and observed secondary structure of T4 phage lysozyme, Biochimica et Biophysica Acta (BBA) - Protein Structure, 405, 442–451, doi:10.1016/0005-2795(75)90109-9, 1975.

5 Medrzycka, D., Benn, D. I., Box, J. E., Copland, L., and Balog, J.: Calving Behavior at Rink Isbræ, West Greenland, from Time-Lapse Photos, Arctic, Antarctic, and Alpine Research, 48, 263–277, doi:10.1657/AAAR0015-059, 2016.

Messerli, A. and Grinsted, A.: Image georectification and feature tracking toolbox: ImGRAFT, Geoscientific Instrumentation, Methods and Data Systems, 4, 23–34, doi:10.5194/gi-4-23-2015, 2015.

Motyka, R. J., Dryer, W. P., Amundson, J., Truffer, M., and Fahnestock, M.: Rapid submarine melting driven by subglacial discharge, LeConte

10   Glacier, Alaska, Geophysical Research Letters, 40, 5153–5158, doi:10.1002/grl.51011, 2013.

Murray, T., Selmes, N., James, T. D., Edwards, S., Martin, I., O'Farrell, T., Aspey, R., Rutt, I., Nettles, M., and Baugé, T.: Dynamics of glacier calving at the ungrounded margin of Helheim Glacier, southeast Greenland, Journal of Geophysical Research: Earth Surface, 120, 964–982, doi:10.1002/2015JF003531, 2015.

Nick, F., Van der Veen, C. J., Vieli, A., and Benn, D.: A physically based calving model applied to marine outlet glaciers and implications

15   for the glacier dynamics, Journal of Glaciology, 56, 781–794, doi:10.3189/002214310794457344, 2010.

Nuth, C., Kohler, J., König, M., von Deschwanden, A., Hagen, J. O., Kääb, A., Moholdt, G., and Pettersson, R.: Decadal changes from a multi-temporal glacier inventory of Svalbard, The Cryosphere, 7, 1603–1621, doi:10.5194/tc-7-1603-2013, 2013.

Ojala, T., Pietikäinen, M., and Harwood, D.: A comparative study of texture measures with classification based on featured distributions, Pattern Recognition, 29, 51–59, doi:10.1016/0031-3203(95)00067-4, 1996.

20 Ojala, T., Pietikäinen, M., and Maenpaa, T.: Multiresolution gray-scale and rotation invariant texture classification with local binary patterns, IEEE Transactions on pattern analysis and machine intelligence, 24, 971–987, doi:10.1109/TPAMI.2002.1017623, 2002.

O'Neel, S., Marshall, H. P., McNamara, D. E., and Pfeffer, W. T.: Seismic detection and analysis of icequakes at Columbia Glacier, Alaska, Journal of Geophysical Research: Earth Surface, 112, doi:10.1029/2006JF000595, 2007.

Pietikäinen, M., Hadid, A., Zhao, G., and Ahonen, T.: Local Binary Patterns for Still Images, pp. 13–47, Springer London, London,

25   doi:10.1007/978-0-85729-748-8_2, 2011.

Rignot, E., Fenty, I., Xu, Y., Cai, C., and Kemp, C.: Undercutting of marine-terminating glaciers in West Greenland, Geophysical Research Letters, 42, 5909–5917, doi:10.1002/2015GL064236, 2015.

Schild, K. M. and Hamilton, G. S.: Seasonal variations of outlet glacier terminus position in Greenland, Journal of Glaciology, 59, 759–770, doi:10.3189/2013JoG12J238, 2013.

30 Schild, K. M., Hawley, R. L., Chipman, J. W., and Benn, D. I.: Quantifying suspended sediment concentration in subglacial sediment plumes discharging from two Svalbard tidewater glaciers using Landsat-8 and in situ measurements, International Journal of Remote Sensing, 38, 6865–6881, doi:10.1080/01431161.2017.1365388, 2017.

Stehman, S. V.: Selecting and interpreting measures of thematic classification accuracy, Remote Sensing of Environment, 62, 77–89, doi:10.1016/S0034-4257(97)00083-7, 1997.

35 Straneo, F. and Heimbach, P.: North Atlantic warming and the retreat of Greenland's outlet glaciers, Nature, 504, 36–43, doi:10.1038/nature12854, 2013.

Torr, P. and Zisserman, A.: MLESAC: A New Robust Estimator with Application to Estimating Image Geometry, Computer Vision and Image Understanding, 78, 138–156, doi:10.1006/cviu.1999.0832, 2000.

Truffer, M. and Motyka, R. J.: Where glaciers meet water: Subaqueous melt and its relevance to glaciers in various settings, Reviews of Geophysics, 54, 220–239, doi:10.1002/2015RG000494, 2015RG000494, 2016.

Vallot, D., Åström, J., Zwinger, T., Pettersson, R., Everett, A., Benn, D. I., Luckman, A., Van Pelt, W. J. J., and Nick, F.: Effects of undercutting and sliding on calving: a coupled approach applied to Kronebreen, Svalbard, The Cryosphere Discussions, 2017, 1–25, doi:10.5194/tc-2017-166, 2017.

Van der Veen, C.: Calving glaciers, Progress in Physical Geography, 26, 96–122, doi:10.1191/0309133302pp327ra, 2002.

Walter, F., O'Neel, S., McNamara, D., Pfeffer, W. T., Bassis, J. N., and Fricker, H. A.: Iceberg calving during transition from grounded to floating ice: Columbia Glacier, Alaska, Geophysical Research Letters, 37, doi:10.1029/2010GL043201, 2010.

Warren, C., Benn, D., Winchester, V., and Harrison, S.: Buoyancy-driven lacustrine calving, Glaciar Nef, Chilean Patagonia, Journal of Glaciology, 47, 135–146, doi:10.3189/172756501781832403, 2001.

Westrin, P.: External Conditions Effects on the Self-Organised Criticality of the Calving Glacier Front of Tunabreen, Svalbard, Master's thesis, Uppsala University, Department of Earth Sciences, 2015.

Zheng, Y., Zhang, X., Hou, B., and Liu, G.: Using Combined Difference Image and k-Means Clustering for SAR Image Change Detection, IEEE Geoscience and Remote Sensing Letters, 11, 691–695, doi:10.1109/LGRS.2013.2275738, 2014.